Discover Materials

Research

MICP treated sand: insights into the impact of particle size on mechanical parameters and pore network after biocementation

N. Erdmann[1] · S. Schaefer[2] · T. Simon[1] · A. Becker[3] · U. Bröckel[2] · D. Strieth[1]

Received: 28 May 2024 / Accepted: 5 August 2024
Published online: 20 September 2024

Abstract

Microbiologically Induced Calcium Carbonate Precipitation (MICP) is a technology for improving soil characteristics, especially strength, that has been gaining increasing interest in literature during the last few years. Although a lot of influencing factors on the result of MICP are known, particle size and shape of the particles remain poorly understood. While destructive measuring of compressive strength or calcium carbonate content are important for the characterization of samples these methods give no insight into the internal structures and pore networks of the samples. X-ray microcomputed tomography (micro-CT) is a technique that is used to characterize the internals of rocks and to a certain degree MICP-treated soils. However, the impact of filtering and image processing of micro-CT Data depending on the type of MICP sample is poorly described in the literature. In this study, single fractions of local quarry were treated with MICP through the ureolytic microorganism *Sporosarcina pasteurii* to investigate the influence of particle size distribution on calcium carbonate content, unconfined compressive strength and the reduction of water permeability. Additionally, micro-CT was conducted to obtain insights into the resulting pore system. The impact of the Gauss filter und Non-local means filter on the resulting images and data on the pore network are discussed. The results show that particle size has a significant impact on the result of all tested parameters of biosandstone with lower particle size leading to higher strength and generally higher calcium carbonate content. Micro-CT data showed that the technology is feasible to gain valuable insights into the internal structures of biosandstone but the resolution and signal-to-noise ratio remain challenging, especially for samples with particle sizes smaller than 125 µm.

Article highlights

- Microbiologically Induced Calcium Carbonate Precipitation is more effective for smaller sand particle sizes
- Smaller particle size of sand lead to higher permeability reduction, higher compressive strength and higher calcium carbonate contents in biosandstone
- X-ray microcomputed tomography and image analysis is sufficient to characterize the pore system of biosandstone and detect uneven biocemented areas
- Usage of different digital filters influence resulting images and data from X-ray microcomputed tomography

Supplementary Information The online version contains supplementary material available at https://doi.org/10.1007/s43939-024-00108-3.

✉ D. Strieth, d.strieth@googlemail.com | [1]Chair of Bioprocess Engineering, University of Kaiserslautern-Landau, Kaiserslautern, Germany. [2]Environmental Campus Birkenfeld, Institute of Microprocess Engineering and Particle Technology, University of Applied Sciences Trier, Birkenfeld, Germany. [3]Chair of Soil Mechanics and Foundation Engineering, University of Kaiserslautern-Landau, Kaiserslautern, Germany.

Keywords Microbiologically induced calcium carbonate precipitation (MICP) · *Sporosarcina pasteurii* · X-ray microcomputed tomography (micro-CT) · Image analysis · Gauss filter · Non-local means filter · Pore network

1 Introduction

Microbiologically Induced Calcium Carbonate Precipitation (MICP) is a technology that got more and more attention in research during the last years [1]. Through different microbiological pathways calcium carbonate is precipitated. The most used pathway is still the ureolytic MICP. Ureolytic microorganisms hydrolyse urea to ammonium-ions and carbonate-ions (Eq. 1) while the latter will be precipitated in the presence of calcium-ions as calcium carbonate ($CaCO_3$) (Eq. 2).

$$CO(NH_2)_2 + 2H_2O \rightarrow CO_3^{2-} + 2NH_4^+ \tag{1}$$

$$CO_3^{2-} + Ca^{2+} \rightarrow CaCO_{3(s)} \tag{2}$$

This $CaCO_3$ can form bridges between particles and act as a binder and can therefore improve mechanical parameters of different soil types. Researchers have shown the potential of MICP to improve compressive strength [2, 3], liquefaction resistance [4, 5] and resilience against wind erosion [6] of soils. Furthermore, it can be used to improve compressive strength and reduce water permeability [7, 8] of existing construction materials. Through this process it is also possible to produce novel, artificial sandstone like materials. Although MICP based materials are not yet ready to be used for construction, they can be used for research purposes [9] which opens up a new field of study. Regardless of the intended use case of biocemented soils, the homogeneity of calcium carbonate distribution in the sample is important to evaluate the quality of the cementation. Most studies use cyclic application of a calcination solution (Urea/Calcium salts) and bacteria suspension (ureolytic microorganisms) to achieve biocementation. This often leads to clogging and inhomogeneous samples. It is possible to estimate sample homogeneity through measurements of calcium carbonate content or compressive strength content in different sections of the biosandstone which has been done several times in literature [10–12]. But these results are limited to sections of consolidated samples and do not yield information about small local inhomogeneities or uniformity from the outer layers of the sample to the core. Since mechanical parameters of biosandstone correlate with the calcium carbonate content in the sample [12–14], reproducible results for MICP will therefore largely depend on achieving a homogenous calcium carbonate distribution. Research has described several biological, chemical and physical parameters that impact the final results of MICP [1, 15]. While a lot of these parameters like type and concentration of bacterial cells, temperature, composition of calcination solution, etc. can be controlled, the influence of the particle size distribution of sand dictates if the locally available sand source is suitable for MICP. Although research on the influence of particle size and shape of sand acknowledges the importance of these parameters on the result of MICP the understanding of these effects remains limited [9]. Measuring mechanical parameters and calcium carbonate content of biosandstone after MICP can only give limited insight in intrinsic effects that lead to these observed characteristics. It is therefore necessary to improve our understanding of the internal structures and the pore network of biocemented materials and their resulting influence of e.g. unconfined compressive strength (UCS) or water permeability.

By using X-ray microcomputed tomography (micro-CT) it is possible to analyze materials destruction free. Therefore, X-ray images of the samples are taken based on the attenuation of X-rays due to density differences, differences in atomic numbers or phase boundaries. After reconstruction, images with distribution of grey values can be analyzed by 2D and 3D image analysis. This makes it possible to gain detailed insights into the inner structure of these samples. Scientists have analyzed different types of natural sandstone with X-ray CT [16–18] also MICP was characterized by CT [19–25]. While all these studies used X-ray CT to investigate MICP with focus on different fields and effects during MICP. Zhou et al. [23] used CT images to study the fracture behavior of single calcareous sand particles that were treated with MICP. Wang et al. [24] went to a bigger scale and focused on analyzing the aggregation patterns of $CaCO_3$ precipitates and to identify efficient cementation patterns. Roy et al. [22] and Terzis et al. [25] used CT images to gain insight into intrinsic properties like pore throats, interparticle contacts and precipitation bonds and connected these information with strength parameters of MICP treated sand. They concluded that not all calcium carbonate bonds equally contribute to the efficiency of MICP treated sand. CT imaging could therefore offer valuable insight in addition to studying only macroscale effects like strength and porosity of MICP treated sand when determining the efficiency of different MICP protocols. This study also tries to bridge CT analysis with parameters like strength, water-permeability and calcium carbonate content of MICP treated sand to further help understanding how the intrinsic parameters are connected with

the macroscopic parameters of MICP treated sand. The examinations of MICP using CT mainly comprised the sandstone structure, the pore network, the permeability [1, 22], creation of cracks and potential of crack sealing [40], or degree of calcite precipitation [1]. Various procedures for determining the aforementioned parameters based on image analysis are described in literature. There are different digital filters used to process the CT images and get better signal to noise ratios. At first, the denoising principle based on the replacing of color pixels or grey values with the average of nearby pixels [5]. Using filters, the grey values are processed e.g. with a normal distribution (Gauss filter) or a median of the grey values in the image window or section (Median filter) [24]. Because pixels with same grey value have no reason to be close at all and therefore, the Non-local Means filter uses the entire image for comparison of each pixel [5]. Also weighing factors are used at this filter [26].

For image analysis of CT images of sandstone or MICP sandstone Kirkland et al. [26] and Huang et al. [27] use Gauss filter, while Zhao et al. [28] and Wang et al. [24] use a Median filter. In contrast, Schlüter et al. [29], Schmitt et al. [18], Thomson et al. [30], Sun et al. [31], Peltz et al. [32]and Su et al. [33] use the Non-local means filter (NLM). Gong et al. [17] show that the images look very different when Gauss, NLM, anisotropic diffusion or Mean filters are used. This research group found the NLM filter to be the most suitable and carried out the image analysis with it. What all these publications have in common is that the results without/with the use of the filter or the use of different filters are not shown in their effects on the image analysis results, but the filters are only considered as part of the image analysis. Filters have an influence of the grey value distribution in images by e.g. shifting the distribution and therefore have an impact of what remains for the subsequent image analysis. This paper gives both, an overview about the visual effects of the applied filters but also the differences in resulting pore network of the MICP sandstone.

In this work, we present the influence of different grain sizes of sand on calcium carbonate content, water permeability and unconfined compressive strength (UCS). Simultaneously utilizing micro-CT to gain insight into the biosandstone and its internal pore network. Additionally, a comparison of different digital filters was performed to evaluate their influence on the quality of the image processing of CT images.

2 Materials and methods

2.1 Cultivation of *Sporosarcina pasteurii*

During this study, *Sporosarcina pasteurii* (ATCC 11859) was used as an ureolytic microorganism for MICP. For cultivation of *S. pasteurii* the culture medium for according to ATCC was used. The medium contained 20 g L^{-1} yeast extract (Carl Roth, Germany), 15.75 g L^{-1} TRIS-buffer (Carl Roth, Germany) and 10 g L^{-1} ammonium sulfate (VWR International, USA). For media preparation TRIS-Buffer was adjusted to pH 9.2 and then split into two parts: ammonium sulfate was added to one part and yeast extract to the other. The two parts were then separately autoclaved and after cooling combined under sterile conditions. *S. pasteurii* was incubated in 500 mL erlenmeyer flasks without baffles with a filling volume of 200 mL at 30 °C and at 250 rpm (Multitron S-000115689, Infors HT, Switzerland) until the cells reached late exponential phase. The cells were then harvested and washed 3 times with 0.9% NaCl. Centrifugation after each washing step was performed at 10 °C for ten minutes at 4000 rpm. Cells were then resuspended in 0.9% NaCl (Carl Roth, Germany), to an OD_{600} of 3.5 and stored at 4 °C until cementation experiments. Additional to OD_{600} the ureolytic activity of *S. pasteurii* was determined by conductivity method as described by Whiffin [34].

2.2 Sand types for cementation experiments

For cementation experiments two sands were investigated. SH (Sand Haltern) is a silica sand from Haltern (Quarzwerke Haltern GmbH, Haltern, Germany) that was used in previous studies for MICP [35]. SP (Sand Picard) is waste sand from a Sandstone Quarry (Carl Picard Natursteinwerk GmbH, Krickenbach, Germany). The particle size distribution (PSD) of 500 g of the sands was determined after wet sieving and drying for 24 h at 105 °C with sieves (Diameter 200 mm, RETSCH GmbH, Germany) with mesh size between 0.063 and 16.0 mm (Table 1). Each sample is named by the name of the sand type (SH, SP) and the particle size (0063, 0125, 0250, 0500, Mix) for example SP0250 is the fraction with $d_{max} = 0.250$ mm from the sand from the Sandstone quarry Picard (SP). Additionally, the particle size distribution (PSD) of SH was replicated from fractions of the Sands SP to compare different sand types with nearly identical PSD. This recreation is called "SPMix".

Table 1 Overview of PSD from the Sand SH, SP, and SP after mixing to achieve the same PSD as SH

Particle size in mm		Mass percentage of the particle fraction in %		
d_{min}	d_{max}	SH	SP	SP Mix
0.0	0.063	4.61	15.28	4.61
0.063	0.125	1.87	6.40	1.87
0.125	0.25	75.81	30.41	75.81
0.25	0.5	17.7	39.31	17.7
0.5	1.0	0.01	7.56	0.01
1.0	2.0	0.00	1.03	0.00
2.0	4.0	0.00	1.18	0.00
4.0	8.0	0.00	2.25	0.00
8.0	16.0	0.00	2.33	0.00

d_{min} and d_{max} give the lowest and highest range of particle size that can pass the sieves

2.3 Preparation of sand columns

Sand columns were prepared in two sizes to meet the different size requirements of the analytical methods. For unconfined compressive strength and water permeability tests sand columns were prepared from 50 mL reaction tubes, diameter 27 mm (Greiner centrifuge tubes, Sigma-Aldrich). The bottom part of the tube was cut off and five holes (diameter 6 mm) were drilled in the cap to allow liquids to flow freely through the column. Prior to filling the columns with sand, the holes were covered with filter paper (40 µm. Qualitativ Filterpapier 417, VWR International). For micro-CT smaller samples were necessary due to the size of the detector of the utilized CT device (see Sect. 2.6). Therefore, molds were prepared from the top part of 10 mL standard Pasteur pipettes not graded 300 mm (Carl Roth, Germany). They were cut at the top and the bottom part was shortened to 1 cm to allow better handling of the columns. The outlet of the pipette was sealed with cotton. The conical part of the pipette was filled with sand SH as drainage. A non-woven all-purpose cloth (84% viscose, 16% polypropylene, W5, Germany) was placed on this drainage sand. The columns were filled with sand through a funnel that was placed roughly 1 cm above the molds. 40 g sand for the big samples and 5 g sand for the small samples was poured slowly through the funnel into the mold. The sand was covered with filter paper as well to prevent disturbing the surface of the sand column during MICP. Afterwards, the columns were closed with a plug containing a hole for the application of bacteria suspension and calcination solution during MICP.

Additionally, the bulk density of the loosely filled sand was determined in 20 mL metal cylinders with a diameter of 27 mm. Therefore, sand was prepared in the same way as for the MICP molds and the excess sand from top was removed with a metal plate (N = 5). After weighting the sand, the bulk density of the sand was calculated as g/cm^3. The obtained bulk densities were as follows: SH (1.47 ± 0.02 g/cm^3) SPMix (1.38 ± 0.01 g/cm^3), SP0063 (1.25 ± 0.02 g/cm^3), SP0125 (1.39 ± 0.01 g/cm^3), SP0250 (1.46 ± 0.02 g/cm^3), SP0500 (1.43 ± 0.03 g/cm^3). Except SP0063 all of these densities lie within 5% of the average of 1.39 g/cm^3 while SP0063 deviates 10% from this average.

2.4 MICP Protocol for biocementation

MICP treatment was conducted as surface percolation method through sequential injection of resuspended cell suspension (OD_{600} = 3.5) and a calcination solution containing 1492 mM urea (Fisher Scientific, USA) and 1392 mM calcium chloride dihyadrate (Carl Roth, Germany). A schematic overview of the process can be seen in Fig. 1).

Initially, 50% pore volume of cell suspension was applied on top of the column with a peristaltic pump (IPC 8, ISMATEC, Switzerland) with a flow rate of 3 mL min^{-1}. After 2 h 50% pore volume of calcination solution was applied at 3 mL min^{-1}. Since the percolation of liquid into the sample decreases with additional MICP cycles due to clogging this time between the applications was necessary to give the cell suspension enough time to percolate into the sample during the last cycles of the treatment. The application of calcination solution was followed by 5 h of incubation at 25 °C to give the reaction time to form calcium carbonate. This treatment is considered as one cycle with 10 cycles in total for each column. 10 cycles were chosen because preliminary experiments showed that with 10 cycles we can achieve a reasonable strength of the samples while clogging of the samples started to occur from 10 cycles onwards which lead to uneven cementation and a wider variance of compressive strength (Supplement 7). After the last cycle columns were washed with 300% pore

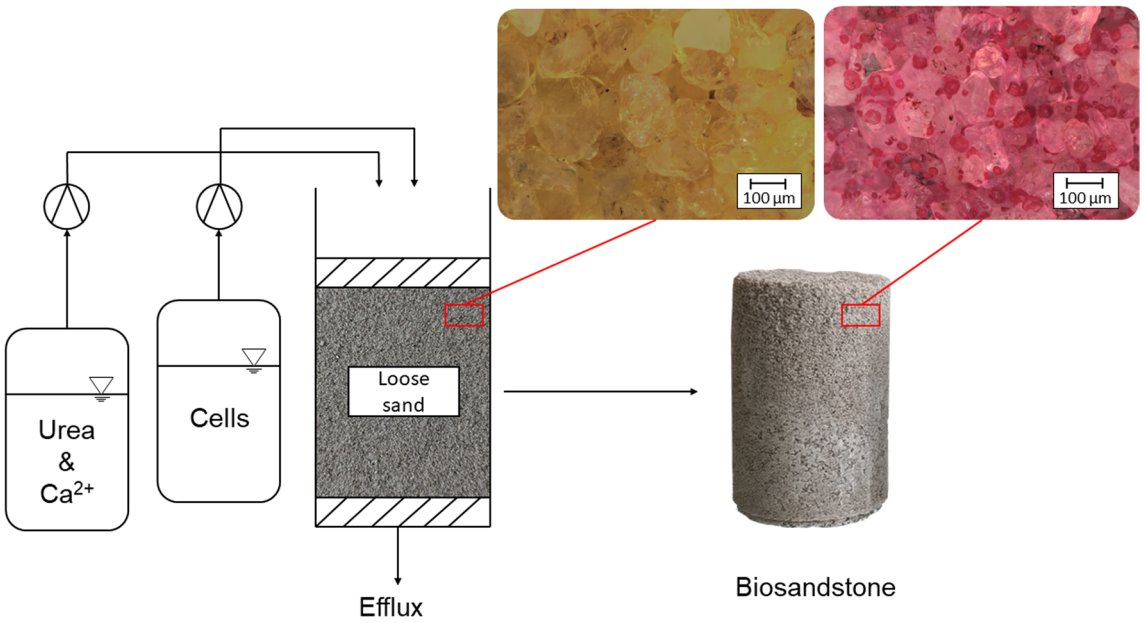

Fig. 1 Schematics of biosandstone production. Microscopic images show the surface of loose sand and biosandstone after staining calcium carbonate crystals with Alizarin Red S (Carl Roth, Germany)

volume of distilled water to flush out residual salts and cells and dried for 72 h at 60 °C. After curing at room temperature for 14 days unconfined compressive strength and permeability tests were performed.

2.5 Determination of calcium carbonate content

For calcium carbonate determination 5 g of the sample were mixed with 20 mL of 2 M hydrochloric acid. Once no production of CO_2 gas could be visually observed the reaction was given another hour to dissolve any remaining calcium carbonate. Afterwards the samples were diluted in 2 mM nitric acid and the content of soluble calcium ions was determined by ion exchange chromatography (n 930 Compact IC Flex, METROHM GmbH & Co. KG). Based on the concentration of soluble calcium ions the total amount of calcium carbonate in the sample was calculated and the content in % calculated as the quotient of calcium carbonate over the initial sample weight.

2.6 Image acquisition by X-ray microcomputed tomography

To get a better resolution on micro-CT, the smaller samples (diameter about 10 mm) were used as mentioned in section 2.3. The list of the sample labels can be found in Table 2. Depending on the sample diameter, a scan resolution of 6.79 µm/pixel was achieved. With 90 kV and 110 µA as well as a 0.25 mm aluminum filter and an exposure time of 3012 ms the samples were X-rayed at 0.3° angle steps. Scan duration was about three hours in a skyscan 1272 X-ray microtomograph (Bruker, Kontich, Belgium). To reduce noise, a frame averaging of 4 was applied.

Thereafter the reconstruction was performed by using NRecon 2.0.0.5 (Bruker, Kontich, Belgium). Here postalignment was 1, no smoothing was applied, ring artefacts reduction was set to 50 although there were less to none visible. Min and max image conversion were set to 0 resp. 0.077945. Images were reconstructed as tiff 16 images.

Table 2 Overview of micro-CT samples

Sample label	Particle size in mm	Weight in g	Calculated object height in volume of interest in mm
SP0063	> 0.063	5.01	10.054
SP0125	> 0.125	5.02	10.570
SP0250	> 0.250	5.03	10.183
SP0500	> 0.500	5.02	10.257

2.7 Determination of water permeability

Water permeability was determined as the coefficient of permeability k_f by Darcy´s law. The measurement was conducted at test station compliant with DIN EN ISO 17892–11 [36]. The test station includes a pressure-controlled tank made of polyvinyl chloride. The pressure in the pressure tank is set to a constant value of p = 0.5 bar by a compressor, which is regulated by a pressure gauge. The container is a tube that is screwed to a teflon top and bottom section using threaded rods. The samples are measured using modified centrifuge tubes. These are positioned in the centre of the pressure vessel. Filter disks made of sintered bronze with a layer thickness of 2 mm are placed above and below the sample or the loose bulk material. The centrifuge tube is screwed into a thread in the base section. The upper opening of the tube is closed using a silicone plug in which a silicone tube is positioned. The flow rate of water is set manually in the range 2–200 mL min^{-1}. Once a stationary flow regime through the sample has been established, the amount of liquid passed per time can be measured. The measurement duration of the liquid volume was five minutes with one measurement being carried out every minute. The quantity of liquid that passes through is collected in a container and the mass was determined using a digital scale. The coefficient of permeability k_f was calculated with the equations of Darcy´s law (Eqs. 3–5).

$$\Delta h_W = i \cdot H_P \tag{3}$$

$$v = \dot{V} \cdot A^{-1} \tag{4}$$

$$k_f = v \cdot i^{-1} \tag{5}$$

Using the measured sample height H_P and a self-selected hydraulic gradient i, the hydraulic pressure difference Δh_W can be calculated (Eq. 3). This is required to set the pressure applied to the pressure gauge. The flow velocity v is then calculated using the volume flow $\dot{V}$, which is determined by the individual measurements, and the cross-sectional area A of the biosandstone sample (see Eq. 4). Finally, the permeability coefficient k_f is determined using the flow velocity v and the hydraulic gradient i (see Eq. 5).

2.8 Determination of unconfined compressive strength

Unconfined compressive strength (UCS) was determined with a universal testing stage (Compression Testing Machine Type 812, FHF Strassentest, Germany). Before measurement the top of samples were sanded flat to achieve an even surface for force application during measurement. The final height of the samples H_P were 40 ± 5 mm. Force was applied with a traverse speed of 2 mm min^{-1} until the sample broke. From the resulting stress–strain diagrams the UCS was determined.

2.9 Image analysis

First of all, the Volume of Interest (VOI) is determined. Due to the sample setup inside the pipette with the loose sand or MICP sandstone between filter paper and non-woven cloth, the amount of images in one stack varies. The separation objects filter paper or non-woven cloth can lie in an angle and therefore, the images for image analysis have to be chosen wisely. For the analysis, only images without pipette walls, filter paper or non-woven cloth are used. Despite efforts to keep deviations as small as possible, the mean of images in one stack is about 1511 ± 28 images. This results in an object height of 10.266 ± 0.19 mm for MICP sandstone characterized with micro-CT. After the VOI determination, the image analysis can be started. Therefore, either no filter, Gauss filter or Non-local means filter were applied. No filter gives the reference, while Gauss filter is quite popular and part of many image analysis softwares. So it is a good option to compare it to other digital filter results. And Non-local means filter was chosen because of the fact, it uses the entire image not just surrounding pixels for comparison of grey values and their adjustment.

The image analysis was performed with CTAnalyser V1.20 (Bruker. Kontrich, Belgium). Gauss filtering is possible with CTAnalyser (CTAn), while Non-Local Means (NLM) has to be performed with Fiji, an open source image processing package basing on ImageJ2. In Fiji it is possible to use the Non-local means plug-in based on the work of Buades et al. [37] and Darbon et al. [38]. NLM was performed with Sigma = 15. Afterward, a lot of noise, especially in sand grains, is removed. But it has to be kept in mind, that filters maybe cause artefacts, which are then part of the image analysis and results. For the image analysis with CTAn two task lists are necessary. In the first task list, sandstone volume and porosity of the

object are calculated. The second task list is all about analysing pore space between sand grains. Of interest here are either the connected pores, which form a coherent pore system, or the individual pores. Both task lists can be found in supplementary material (Supplement 8–11). Figure 2 illustrates the process of image acquisition to image analysis of sandstone and the determination of the connected pore network (CPN) and individual pores. First of all, the different filters or no filter was applied to the grey value images of the volume of interest. Then, when noise is removed, the biosandstone can be extracted by setting a threshold based on the histogram of the grey value distribution. Afterwards, the binarized images are used to calculate the sandstone volume and object porosity by creating a 3D model out of the 2D image stack using the marching cubes algorithm [39].

To extract the CPN and the individual pores (as shown on Fig. 2, right), first a Region of Interest (ROI) shrink wrap is performed which finishes the first task list. Here, a new region of interest can be created from an existing ROI by adapting the shape of the sandstone object, which was calculated before [40]. An inversion of the sandstone images and a removal of the edge areas forms the basis of the following steps. Bitwise operations and a despeckle step are necessary to separate the CPN from the individual pores. For CPN and individual pores, the calculation of object volume and pore diameter was also performed using marching cubes algorithm.

3 Results and discussion

3.1 Relationship between calcium carbonate content, water permeability, and unconfined compressive strength of biosandstone

The treatment of each sand with MICP resulted in observable calcium carbonate depositions on the sand surface (Fig. 3). In the samples, effective calcium carbonate bridges as well as ineffective crystals that grew into void space could be observed. When observing the figure, the 2D nature of the microscopic image should be kept in mind. It is possible that the ineffective calcium carbonate crystals could be effective in the third dimension. The former effect is the main goal of biocementation through MICP for the improvement of mechanical soil characteristics and the reason for the observed strength of sand after biocementation. The observed quantities of calcium carbonate range from $11.60 \pm 0.25\%$ g g^{-1} to $6.69 \pm 0.59\%$ g g^{-1} of total weight with an overall trend of decreasing calcium carbonate content with increasing particle size (Fig. 5).

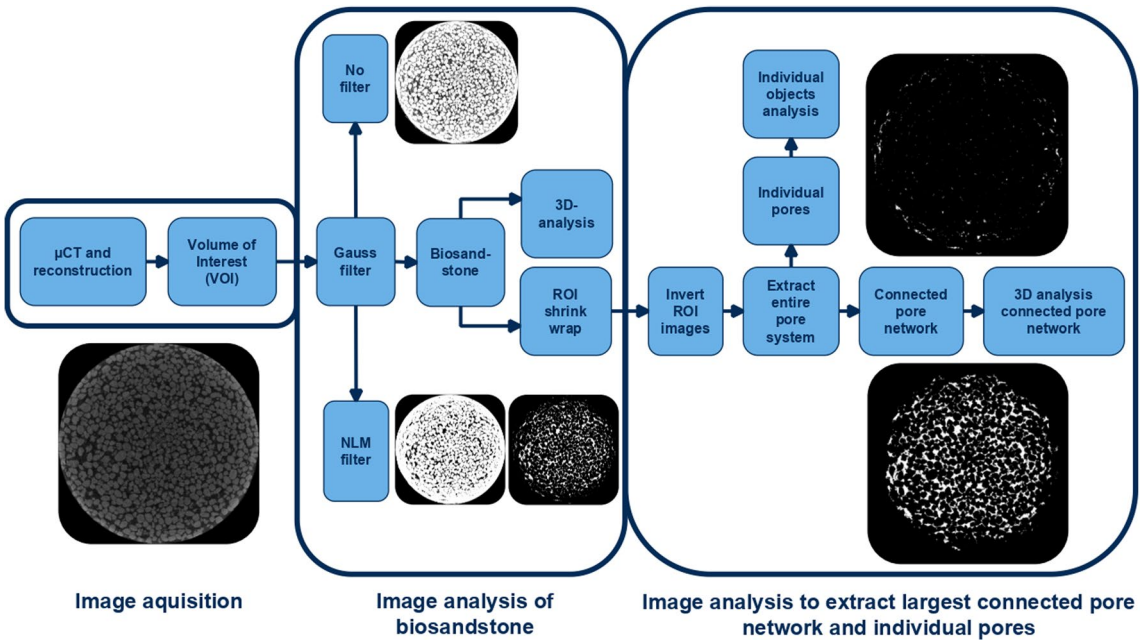

Fig. 2 Scheme of image analysis procedure: The analysis is divided into two task lists where the first task list is used to analyze the sandstone object, and the second one focuses on determining the connected pore network and the individual pores

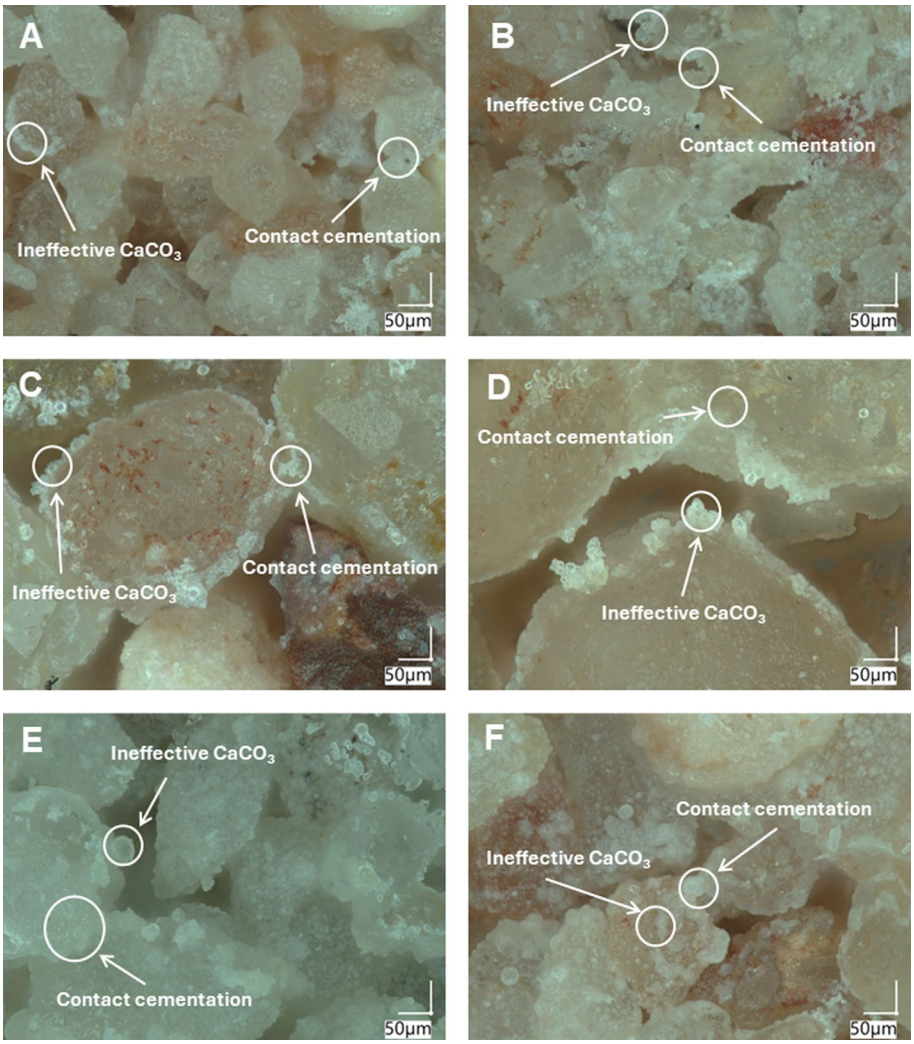

Fig. 3 Microscopic images with 500 × magnification (VHX-7000, Keyence, Germany) of biocemented sand. **A** SP0063; **B** SP0125; **C** SP0250; **D** SP0500; **E**; SH; **F** SPMix

For each sample, there is a decrease in water permeability caused by MICP treatment. For the loose sand and samples treated with MICP, the water permeability is inversely proportional to the grain size (Fig. 4). The water permeability coefficient for the loose sand fraction SP0063–SP0500 ranges from $6.37 \cdot 10^{-5}$ m·s^{-1} to $4.55 \cdot 10^{-4}$ m·s^{-1} and decreases through MICP treatment to $2.12 \cdot 10^{-6}$ m·s^{-1} (SP0063) to $2.50 \cdot 10^{-4}$ (SP0500). The reduction of permeability ranges therefore from 96.7% (SP0063) to 45.0% (SP0500) and generally decreases with increasing particle size. The strongest decrease from $6.36 \cdot 10^{-5}$ m·s^{-1} to $2.12 \cdot 10^{-6}$ m·s^{-1} occurs for the smallest fraction SP0063. In contrast, the lowest decrease from $4.55 \cdot 10^{-4}$ m·s^{-1} to $2.50 \cdot 10^{-4}$ m·s^{-1} occurs for the largest fraction SP0500. Permeability coefficients of SH and SPMix lie between SP0125 and SP0250, which is because these fractions make up the largest proportion of this fill at 75.8% and 17.7%. Both the two sands SH and SPMix as well as the individual fractions of SP show a reduction in water permeability after MICP treatment of 45.0 to 96.7%. This reduction of permeability through MICP can be attributed to the blocking of flow paths through the sand. Especially large pore networks and channels through the sand get blocked by cementation and permeability is reduced with increasing degree of cementation [40]. The higher decrease for lower particle sizes is most likely attributed to this blocking effect. For smaller particles void space decreases which could lead to calcium carbonate crystals forming with a higher chance at pore throats leading to reduced permeability [9]. Furthermore, for biosandstones with smaller particle size a generally higher degree of cementation was observed (Fig. 5) which also increases the chance of pore blocking.

UCS shows a similar trend for sand fractions. With increasing particle size the UCS of the biocemented samples decreased from 3.04 ± 0.73 MPa (SP0063) to 0.74 ± 0.15 MPa (SP0500) (Fig. 5). Since the void space between particles is bigger for higher particle sizes [9] the formed calcium carbonate crystals have a higher chance of growing into voids

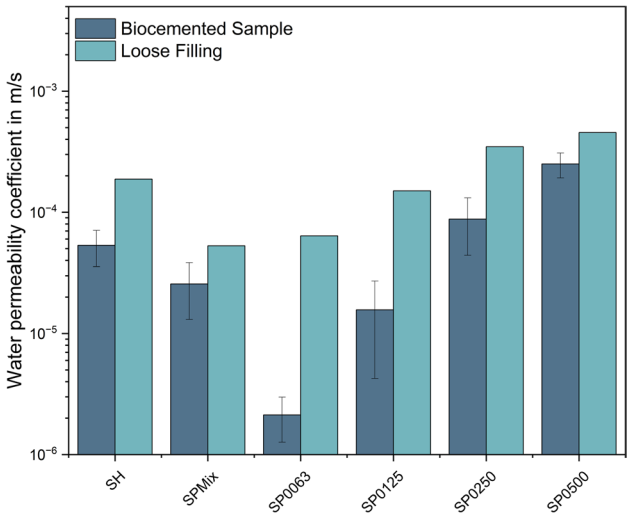

Fig. 4 Water permeability coefficient before and after MICP treatment for different sand fractions. *SH* Sand Haltern, *SP* Sand Picard. The sand fractions were treated with 10 cycles of *S. pasteurii* and calcination solution according to Sect. 2.4. The error represents the standard deviation of n = 6 biological replicates

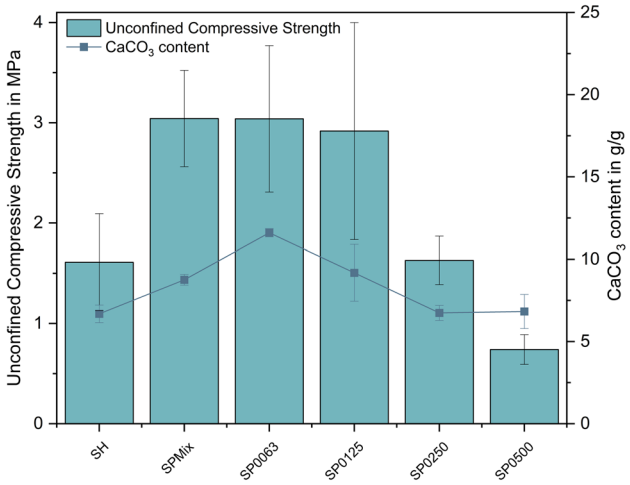

Fig. 5 UCS and CaCO3 content for different sands and particle fractions. For different sand fractions. *SH* Sand Haltern, *SP* Sand Picard. The sand fractions were treated with 10 cycles of S. pasteurii and calcination solution according to Sect. 2.4. The error bars represent the standard deviation of n = 6 biological replicates

instead of forming effective bridges at contact points. SP0063 and SP0125 have nearly identical UCS with SP0125 with higher variances than samples with a bigger particle size which might be due to a higher chance of clogging in the sample which leads to a more uneven distribution of bacteria suspension and calcination solution and therefore uneven calcium carbonate distribution.

This clogging effect is a common phenomenon of MICP calcinated sand although more prominent in sand with low permeability since bacteria suspension and calcination solution can distribute more freely through the sand and therefore the reaction is more evenly distributed throughout the samples [41]. This clogging effect is also likely the reason for the higher decrease in water permeability for smaller particle sizes as the precipitated calcium carbonate blocks pores and thereby flows paths through the sand. The decrease in calcium carbonate content with increasing particle size supports this. Samples with lower particle sizes withhold more calcium carbonate on throat points than samples with bigger particle sizes most likely due to flushing out calcium carbonate from big pores that could not attach to the surface of particles. This effect resulted in higher calcium carbonate content which subsequently resulted in higher UCS and greater reduction of permeability. It is notable, that by reconstructing the particle size distribution of SH with SP did not lead to similar UCS or reduction of permeability coefficient. With 3.04 ± 0.48 MPa and a reduction of permeability of 51.31% SPMix had a significantly higher UCS compared to SH (1.61 ± 0.48 MPa) while having a lower reduction in permeability coefficient (71.60%). This suggests that it is not solely the particle size of the sand that impacts the result but also the type of sand. Particle shape and size might be of similar importance. A study conducted by Song et al. investigated MICP-treated silica sand with different particle morphologies and gradings from three sand types sieved into four size fractions: (1.00–0.85 mm), (0.85–0.425 mm), (0.425–0.250 mm), (0.250–0.180 mm) [42]. They observed that UCS of treated spherical and near-spherical sands peaked at 5.21 MPa for particle sizes of 0.85–0.425 mm, whereas treated angular sands

had increasing UCS with decreasing particle size. Similar to our findings, they observed an increase of calcium carbonate content with decreasing particle size for all tested sand types. They concluded that particle morphology and resultant bonding mechanisms exert critical controls in MICP-grouting that significantly affect the cementation structure and, as a result, the ensemble strength of the treated assemblage. Gowthaman et al. consolidated three well-graded sands Mizunami (d_{50} = 1.6 mm), Mikawa (d_{50} = 0.87 mm), and Toyoura (d_{50} = 0.2 mm), and achieved compressive strengths of 1.82 MPa. 2.67 MPa and 3.98 MPa respectively [43]. Zhao et al. observed a notable reduction in permeability and improvement in UCS with the incorporation of different fine particle contents and pore ratios in silt [44]. Although our understanding of the mechanisms behind the impact of grain size and shape of particles on the process remains limited [9], the importance of particle size on UCS, permeability reduction, and calcium carbonate content of biocemented sand when choosing sand for MICP is clear. In summary, our research findings are in alignment with recent literature, indicating that the efficacy of MICP in improving UCS, reducing water permeability, and influencing calcium carbonate content is significantly affected by sand particle sizes. These insights not only validate our research outcomes but also highlight the necessity of precise knowledge of the soil that will be utilized for MICP. Although the macroscopic measurements of UCS, calcium carbonate content, and permeability hold valuable information on the efficiency of the MICP process it remains important to gather information on the internal structure of biocemented sand that cannot be explained by these measurements. CT image analysis is a tool that could help extend our understanding of the internals of biocemented sand.

3.2 CT results

Images of biosandstone, created by X-ray microcomputed tomography and image analysis, were first of all processed with or without a digital filter. Afterwards, image analysis was performed with the two task lists (Supplement 8–11). Resulting images can be separated by their containing objects like sandstone, connected pore system or individual pores. A comparison of image components like sandstone, pore network, or edge areas shows: Whether or not a filter is used, the sandstone has an average proportion of about 63% of the image, while the pores have about 13.5–14.9% as can be seen in Fig. 6. The rest are edge areas, which exist due to the round sample geometry.

Figure 6 shows exemplarily 2D images the results of image analysis by displaying sandstone and pore network, consisting of connected pores and individual pores. Analysed was the entire sample in 3D, where the marching cubes algorithm, developed by Lorensen et al. [39], created a 3D Volume out of the 2D image stack. The object(s) of interest, respectively sandstone or pores, were afterwards used to determine parameters like sandstone volume, porosity or pore volumes.

For a better visualization, Fig. 6 presents 2D slides instead of 3D corpses, where especially the individual pores would have been difficult to be seen due to the lack of a spatial resolution in this figure.

Images treated with Non-local means filter show in mean the highest proportion of sandstone and the lowest proportion of pore system. Without a filter, the largest proportion of pores and the smallest proportion of sandstone are present. Noise is probably still present here, which is calculated as pores after setting the threshold and analyzing the image. Table 3 shows the results of image analysis regarding the volumes of either connected pore network or biosandstone, also in comparison with used filters. It can be seen that SP0063 has always the lowest volume of CPN. The reason for this may be that the small sand grains are more densely packed than the sand grains in SP0500. The object volume of biosandstone ranges between 1963 mm^3 up to 2068 mm^3. Differences in the volume of biosandstone regarding the used filters can be recognized.

When analyzing the pore system, it must be noted that there are two ways to achieve the results: CTAn task list 1 calculates the porosity based on the sandstone object, while there is also the possibility to characterize the pores itself to get more information. This is done by the second task list, as described in Sect. 2.9. The detection limit for pores due to the resolution must be taken into account.

Figure 6 shows excerpts of the results of image analysis either of sandstone or CPN and individual pores. The direct characterization of the pores show that there is a large network of connected pores forming the CPN. It can be seen that the individual pores are found more frequently in the edge areas towards the pipette wall at every used sand grain fraction. Whereas the CPN is mainly at the center of the biosandstone. This is particularly interesting about a uniform flow of both, bacteria solution and calcination solution and has also an effect on solidification. Because the solutions should distribute homogeneously through the sand and not just pass through completely. To achieve this, the reaction time must be correct so that there is sufficient time for the cementing reaction. In addition, the cementation should be as uniform as possible through the sample to achieve reproducibility. The micro-CT images provide insight in the biosandstone and enable the detection of optimization potentials. The general visualization of biosandstone can significantly enhance our understanding of the cementation process. Notably, the edges of the

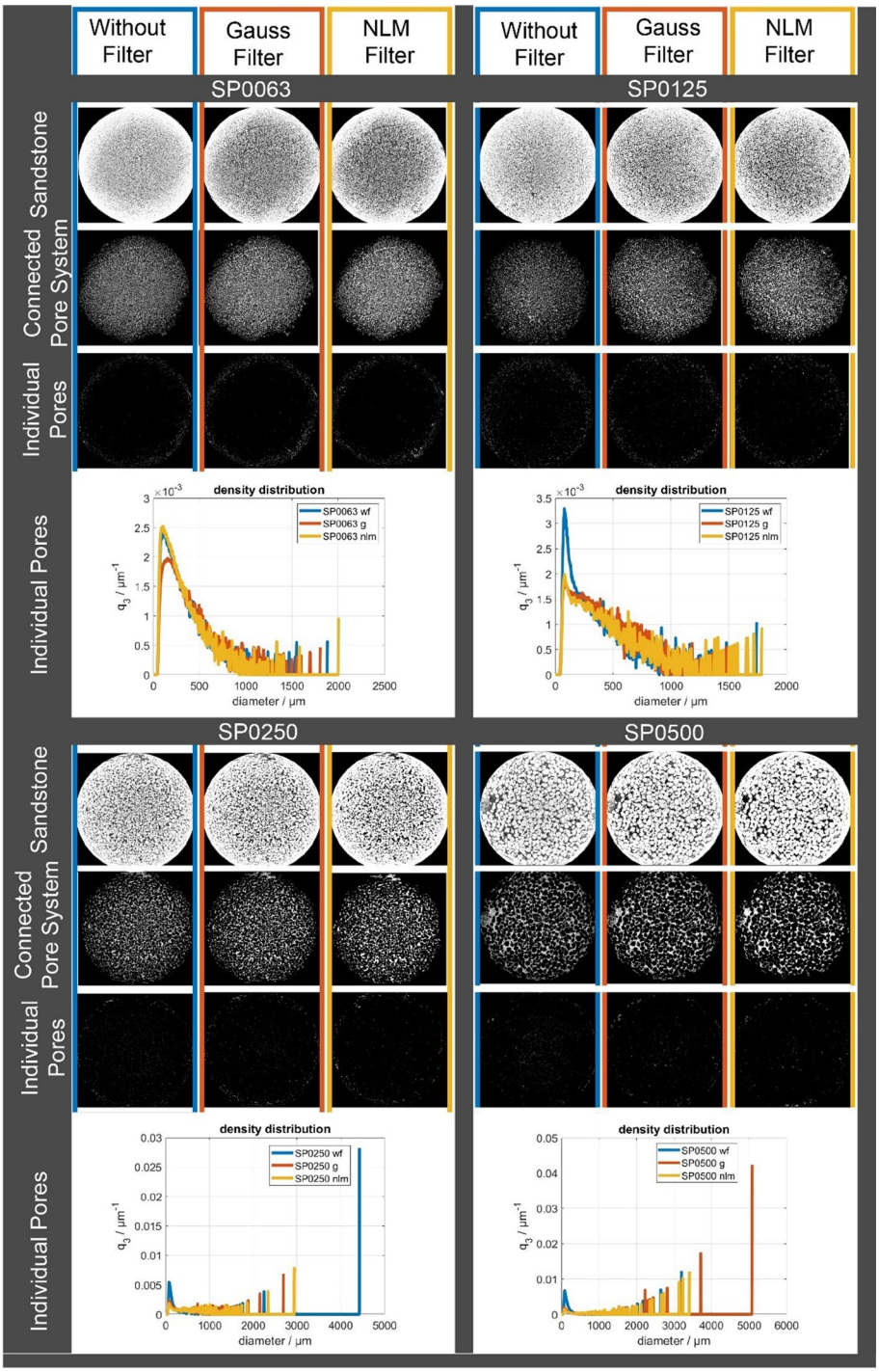

Fig. 6 Results of X-ray microcomputed tomographic characterization and image analysis: Comparison of filter effects and the resulting sandstone object, connected pore network and pores and individual pores. These individual pores are also shown as density distributions of pore volume with *wf* without filter, *g* Gauss filter, *nlm* Non-local means filter. Also, the effect of different sand grain sizes on the difficulty of image analysis can be seen in the binary images

Table 3 Volumes of connected pore network and biosandstone objects calculated by CT and the image analysis

Sample label	Without filter		Gauss filter		NLM filter	
	Connected pore volume in mm^3	Sandstone object volume in mm^3	Connected pore volume in mm^3	Sandstone object volume in mm^3	Connected pore volume in mm^3	Sandstone object volume in mm^3
SP0063	428	1974	446	1963	418	1981
SP0125	466	2061	466	2068	462	2068
SP0250	468	1967	452	1990	453	1998
SP0500	469	1974	453	1999	440	2010

biosandstone show a larger amount of individual pores and a generally higher density of solid material compared to the internal part of the sample (Fig. 6). This observation could be due to a higher formation of calcium carbonate at the edges of the sample which leads to more pore throats being blocked and therefore connected pores being disconnected. The reason for this could be due to a flushing-out effect of residue bacteria cells and small calcium carbonate crystals through the center of the samples with each new cycle of MICP treatment, while more bacteria and crystals being retained in the outer boundaries of the sample. To validate this claim, it would be necessary to gain higher resolution insight into the pore space of the samples, as discussed in Sect. 3.2. Although there is a possibility that this effect could be due to boundary effects of the filtering this case is unlikely since boundary effects influence a zone not larger than twice the particle diameter [45]. The effect of the larger amount of individual pores is observable further into the sample than this effected zone would occur, especially for particle sizes of 63 and 125 µm. Micro-CT measurements offer valuable insight and enable a deeper investigation into the differences between various cementation protocols. For future research, it could be interesting to investigate e.g. the effects of the contact flexible mold on the distribution of calcium carbonate crystals in the biosandstone [46]. During this cementation protocol, the sand is loaded with bacteria suspension and the sample is immersed in a bath of calcination solution. Micro-CT could help to detect how strongly pronounced a cementation gradient from the outer layers to the internal parts of the biosandstone is. Also, it helps to detect defects and large pore systems. These large pore systems can form channels and have a bigger impact on the permeability of sandstone than just the porosity [47]. Also, possible weak points in the sandstone in the form of large pore systems that impact the UCS of biosandstone can be detected by micro-CT. Although it was not possible for us to find a correlation between large pore systems and breaking points of Biosandstone due to the destructive nature of UCS testing, a coupled measurement of UCS and CT scans could be possible to detect initial crack forming. The location of these cracks in the biosandstone would help greatly to improve our understanding of cementation protocols. Whereas the individual pores have also an influence on the biosandstone strength, their influence depends on the pore volume and their number. This is especially important in the context of the correlation of calcium carbonate content, permeability and strength of the biocemented sample. While this study and various research results [19, 48–50] showed that there is a correlation between compressive strength and calcium carbonate content observing the bulk calcium carbonate content will not be enough to describe or reliably predict strength parameters. It is necessary to also include intrinsic information about the efficiency of the bonding of calcium carbonate crystals as described by Dadda et al. [51] or Roy et al. [22]. Dadda et al. [51] focused on differentiating between different types of contact between sand particles (frictional contact, mixed contact and cemented contact) and concluded that for degrees of calcium carbonate most crystals form mixed contacts. Roy et al. [22] on the other hand differentiated between active and inactive bonds of calcium carbonate with a focus of the effects of both bonding types on the result of the MICP. Both studies conclude that there is a necessity to study intrinsic properties of MICP samples which will help to better understand the impact of different MICP treatment strategies on macroscale parameters after treatment.

The nature of bonding and non-bonding particles can also be observed through microscopy as shown in Sect. 3.1 but the use of microscopy is not suitable to determine larger amounts of bonding types through a whole sample compared to CT analysis which allows to compute large amounts of images and data from a single sample. With a resolution of 6.79 µm/pixel during this study a visualization of the bonding crystals was not possible. Although this resolution is sufficient to observe pores (average sizes of 91.7 µm in this study which results in an average of 13.5 pixels per pore diameter) or the sand particles (63–500 µm in this study which results in 9.3 to 73.6 pixel per average particle diameter) the resolution is not suitable to detect smaller calcium carbonate crystals of only a few micrometer. In follow-up studies higher resolution must be achieved, for example by reducing the sample size even further or by diving the smaller samples in subsamples to be able to determine the amount of efficient bonding of the precipitated calcium carbonate. As the understanding of MICP increases it will become more necessary to include information about intrinsic pore systems and the type of calcium carbonate bonds for example through CT or even synchrotron [52] images in studies concerning the optimization of MICP protocols to be able to reliable differentiate between bonding and non-bonding calcium carbonate deposits. Therefore standardized protocols have to be developed to achieve high comparability of these results. This also includes a recommendation on the use of filters for preprocessing the gray value images. Because depending on the filter, changes are made to the gray values by weighting. As soon as the threshold is set, this results in different quantities of voxels that represent the object to be analyzed (sandstone or pore network) as can be seen in Table 4 for individual pores. Here, without a filter a lot of noise is recognized as a pore network, so the use of a sufficient filter is quite useful. The resolution of the images should also be taken into account, especially with small sand grain sizes. Because it is more difficult to distinguish whether there are pores or noise is changing the results.

Table 4 Number of individual pores

Sample label	Without filter Number of individual pores	Gauss filter Number of individual pores	NLM filter Number of individual pores
SP0063	581.020	456.481	468.219
SP0125	398.861	277.628	305.105
SP0250	380.962	171.691	142.371
SP0500	420.214	136.188	100.691

Furthermore, Fig. 6 shows the individual pores as pore volume distributions. There it can be seen, especially for SP0063 and SP0125, that without the use of a filter, the distribution is shifted towards small pore diameters. Additionally, with consideration of the other curve profiles, which show fewer small pores, it can be estimated, that without a filter there is noise in the ROI images, especially for SP0125. It is also noticeable in Fig. 6 that with increasing sand grain size the amount of pores towards higher pore diameters increases. SP0250 and SP0500 show higher pore diameters differences about the used filter. Based on this data, no trends can be seen but to be sure, a higher sample size has to be analyzed. Also, it has to be kept in mind that pore volumina are calculated as spheres and the influence of the pore diameter is high. Therefore, small differences in the filtering process can lead to bigger pores and are shown as peaks in Fig. 6. While the pores of biosandstone are mostly not in the shape of a sphere due to the shape of sand grains and their packing, the assumption of a spherical shape is a simplification to create a working model. The representation as pore distribution curves provides good possibilities for comparison over the entire sample height. In contrast, Minto et al. [21] chose to display the porosity per image along the z-axis to provide an insight into the pore structure in the biosandstone.

In SP0063 there is, regardless of whether a filter was used in the image analysis, the highest proportion of individual pores with about 8.76% (NLM filter) up to 10% (without filter or Gauss filter) of total pore volume. Towards larger sand grains, the proportions become smaller and smaller until it is only 1.39% (NLM filter), 1.48% (Gauss filter), or 2.87% (without filter) for SP0500.

If the entire pore system is considered, it can be seen that the volume of connected pores is lower after using the NLM filter than without the filter (see Table 3), despite otherwise identical treatment of the images. This illustrates the effect of the NLM filter very clearly, as the gray values are averaged here as described above. Some areas that would be counted as pores without the filter are probably influenced by NLM in such a way that they are included at a threshold of 50–255 and counted as sandstone. The use of filters in image analysis and characterization of pore systems has an impact on the results which is shown in Fig. 6. The influence of the filter method varies for different analysis results like the amount of individual pores, volume of connected pores, or total porosity as well as sandstone volume. It is important to mention the filtering method in investigations and consider its effects on calculations. Filters are necessary to reduce visible noise in micro-CT images. The Gauss filter visually reduces noise by smoothing but still retains a high proportion of very fine pores and speckles. On the other hand, the NLM filter performs well, particularly for fractions with larger sand grains. However, it should be noted that the NLM filter produces a noticeable difference from the original image due to the way it changes the gray values, which affects the results when setting the threshold for image analysis.

All in all, the use of a filter for our data is necessary to remove noise. The comparison of Gauss filter and Non-local means filter showed differences in resulting images. Thresholding of this images led to different amounts of sandstone volume or pore network volume. By using the Non-local means filter, a more uniform grey value distribution within the sand grains could be achieved and therefore less speckles within image analysis. It has to be kept in mind, that the sigma parameter must be adjusted to the size of the sand grains depicted so that even the smallest grains of sand and pores are still sharply depicted and are not removed by blurring, if sigma is too large. We recommend using the NLM filter for the application on biosandstone, taking into account the problems and limitations mentioned above.

Further steps in image analysis of the pore network are the determination of pore throats, particle contacts or pores connecting to each other, that are not part of the biggest connected pore network. This analysis is necessary, as research results showed that pore throats play an important role in the efficiency of MICP. This is due to bacteria movement through soil being dependent on the ratio of bacteria size to pore throat size [9, 53, 54] and the fact that formation of calcium carbonate crystals at pore throats seem to correspond to effective $CaCO_3$ cementation [55, 56]. Furthermore, calcium carbonate forming at pore throat has a significant impact on the permeability of the treated samples [57]. Knowledge about pore throats before and after certain treatment cycles during MICP could therefore lead to valuable

insights into phenomena like blocking of the samples at the injection point, which is a common phenomenon during MICP treatment and most likely leading to inhomogeneous treated samples. Therefore, algorithms like Delaunay Tessellation [58], Maximal Ball method [59], Watershed [60] or Medial Axis [61] can be used. Each method has advantages or limitations, which have to be considered for the image analysis process:

- Maximal Ball (MB): Here, spheres are constructed at each voxel of the void until they touch the solid boundaries of the next void. A sphere is a maximal ball, if it is entirely within the material and not contained in another sphere. The spheres of the MC are considered as pores while the minimal balls between the pores are considered as pore throats [62]. This method often leads to an underestimation of throat sizes and also produces tiny and incorrect throats [63].
- Medial Axis (MA): In this method the pore space is transformed into a reduced axis resulting in a topological skeleton along the middle of pore channels [64]. This reduction can be achieved through pore space burning algorithms [65]. After the creation of the skeleton, pore bodies (clusters of void voxels, that are bounded by solid voxels and necks) can be determined [62]. They build the pore space with the constituent pores. A disadvantage of this method is the requirement of a clean-up process afterwards, because noise leads to false positive identification as pores [66]. But MA method allows the preservation of morphological or topological parameters of the pore network [62, 64].
- Delaunay Tessellation (DT): For this method, starting with a packed bed, the pore space is subdivided into a set of tetrahedral volumes with the vertices as the centres of four neighbouring spheres with the void space inside the tetrahedron representing a pore [67]. Then the tetrahedra are merged into larger polyhedrons if single voids were unnecessarily subdivided into multiple ones [68]. To mention hereby is, that the merging of the Delaunay tetrahedra is a subjective criterion and therefore prone to errors, but the throat size can be clearly defined [63].
- Watershed (WA): Here grayscale images are considered as topographic surface based on pixel intensity. Starting from local minima the space is "flooded" until floods coming from two minima come into contact [69]. Because of the "flooding-mechanism", many different pore geometries can be analysed, but often over-segmentation is archived with this method [62].

Further analysis of the pore throats with these algorithms would be suitable to explain some of the observations from Sect. 3.1, especially the stronger reduction of pore size with a smaller particle size of the sand and the higher calcium carbonate content, possibly due to in pore throats retained microorganisms forming more calcium carbonate. Future research on this topic will therefore require CT data with higher resolution to be able to gain further insight into these correlations which will allow researchers to develop new MICP application strategies.

4 Conclusion

In this study, different sand fractions from a local sandstone quarry were consolidated using MICP. The resulting biosandstones were analyzed for unconfined compressive strength, water permeability, and calcium carbonate content. Additionally, the samples were visualized by micro-CT, and the resulting pore system was analyzed. From the results, the following conclusionscan be drawn:

- Sand fractions ranging from 63 to 500 µm as well as ungraded sands could effectively be treated with MICP which resulted in a reduction of permeability coefficient and measurable unconfined compressive strengths (UCS) of biosandstone
- Smaller particle size of sand was better suited for MICP than larger particle size. For smaller sand particles higher UCS, calcium carbonate content and reduction of permeability coefficient could be observed
- Particle size distribution is not the only parameter of sand affecting the efficiency of MICP. Particle shape likely impacts the MICP as well which became apparent by the different results of industrial sand and a reconstruction of the particle size distribution of industrial sand with local quarry sand
- When using locally available sand resources it is necessary to investigate particle size distribution before MICP treatment and eventually reconstruct a more suitable particle size distribution by recombining sand fractions
- X-Ray microcomputed tomography (micro-CT) is suitable for visualization of biosandstone and its pore space but appears to be limited for small particle sizes due to difficulties in differentiating between pore space and noise for certain resolutions. With increasing resolution of the CT there will be more possibilities to switch from visualization of

large pores and uneven areas in the samples towards detailed information about the efficiency of calcium carbonate crystals towards bonding of the sand or the total bonding surface area
- The necessity to include micro-CT visualization and computing in MICP optimization studies will increase. Therefore, suitable protocols for reproducible and comparable data acquisition must be established.
- The choice of filter is important to consider for processing the micro-CT data. Without filtering, noise is apparent in the particle size distribution curves and different filtering changes the results of the observed pore space and porosity

Inhomogeneous areas of biosandstone can be visualized destruction free by micro-CT. This could help to characterize homogeneity of biosandstone in addition to segmented calcium carbonate measurements. In future studies, it could be interesting to investigate if these areas act as breaking points by combining compressive tests with micro-CT measurements

Acknowledgements We thank Martin Picard and the staff of Carl Picard Natursteinwerk GmbH for providing the sand necessary to conduct this research. We would also like to thank Prof. Dr. Christos Vrettos for the opportunity to use the equipment at the department for Soil Mechanics and Foundation Engineering and for his expert input on several occasions.

Author contributions S.S. and N.E. conceived and planned the experiments. Material preparation, data collection, and analysis were performed by S.S, N.E. and T.S.. The manuscript was written by S.S. and N.E. equally. All authors provided critical feedback and input for the manuscript. All authors read and approved the final manuscript.

Funding Open Access funding enabled and organized by Projekt DEAL. This project was financially supported by the Deutsche Forschungsgemeinschaft (DFG. German Research Foundation) – Project-ID 172116086 – SFB 926 and the "Landespotentialbereich NanoKat".

Data availability The data that support the findings of this study are available from the corresponding author upon reasonable request.

Code availability Not applicable.

Declarations

Ethics approval and consent to participate This article does not contain any studies with human participants or animals performed by any of the authors.

Competing interests The authors have no relevant financial or non-financial interests to disclose

References

1. Erdmann N, Strieth D. Influencing factors on ureolytic microbiologically induced calcium carbonate precipitation for biocementation. World J Microbiol Biotechnol. 2022;39:61. https://doi.org/10.1007/s11274-022-03499-8.
2. Liufu Z, Yuan J, Shan Y, et al. Effect of particle size and gradation on compressive strength of MICP-treated calcareous sand. Appl Ocean Res. 2023;140:103723. https://doi.org/10.1016/j.apor.2023.103723.
3. Yuan J, Li Y, Shan Y, et al. Effect of magnesium ions on the mechanical properties of soil reinforced by microbially induced carbonate precipitation. J Mater Civ Eng. 2023. https://doi.org/10.1061/JMCEE7.MTENG-15080.
4. Sharma M, Satyam N, Reddy KR. Liquefaction resistance of biotreated sand before and after exposing to weathering conditions. Indian Geotech J. 2022;52:328–40. https://doi.org/10.1007/s40098-021-00576-x.
5. Shan Y, Zhao J, Tong H, et al. Effects of activated carbon on liquefaction resistance of calcareous sand treated with microbially induced calcium carbonate precipitation. Soil Dyn Earthq Eng. 2022;161:107419. https://doi.org/10.1016/j.soildyn.2022.107419.
6. Dagliya M, Satyam N, Sharma M, et al. Experimental study on mitigating wind erosion of calcareous desert sand using spray method for microbially induced calcium carbonate precipitation. J Rock Mech Geotech Eng. 2022. https://doi.org/10.1016/j.jrmge.2021.12.008.

7. Nasser AA, Sorour NM, Saafan MA, et al. Microbially-induced-calcite-precipitation (MICP): a biotechnological approach to enhance the durability of concrete using *Bacillus pasteurii* and *Bacillus sphaericus*. Heliyon. 2022;8:e09879. https://doi.org/10.1016/j.heliyon.2022.e09879.
8. Chahal N, Siddique R, Rajor A. Influence of bacteria on the compressive strength, water absorption and rapid chloride permeability of fly ash concrete. Constr Build Mater. 2012;28:351–6. https://doi.org/10.1016/j.conbuildmat.2011.07.042.
9. Konstantinou C, Biscontin G, Jiang N, et al. Application of microbially induced carbonate precipitation to form bio-cemented artificial sandstone. J Rock Mech Geotech Eng. 2021;13:579–92. https://doi.org/10.1016/j.jrmge.2021.01.010.
10. Xiao Y, Wang Y, Wang S, et al. Homogeneity and mechanical behaviors of sands improved by a temperature-controlled one-phase MICP method. Acta Geotech. 2021;16:1417–27. https://doi.org/10.1007/s11440-020-01122-4.
11. Cheng L, Cord-Ruwisch R. In situ soil cementation with ureolytic bacteria by surface percolation. Ecol Eng. 2012;42:64–72. https://doi.org/10.1016/j.ecoleng.2012.01.013.
12. Yang D, Xu G, Duan Y. Effect of particle size on mechanical property of bio-treated sand foundation. Appl Sci. 2020;10:8294. https://doi.org/10.3390/app10228294.
13. Chu J, Ivanov V, Naeimi M, et al. Optimization of calcium-based bioclogging and biocementation of sand. Acta Geotech. 2014;9:277–85. https://doi.org/10.1007/s11440-013-0278-8.
14. Zhao Q, Li L, Li C, et al. Factors affecting improvement of engineering properties of MICP-treated soil catalyzed by bacteria and urease. J Mater Civ Eng. 2014;26(12):04014094. https://doi.org/10.1061/(ASCE)MT.1943-5533.0001013.
15. Al Qabany A, Soga K, Santamarina C. Factors affecting efficiency of microbially induced calcite precipitation. J Geotech Geoenviron Eng. 2012;138:992–1001. https://doi.org/10.1061/(ASCE)GT.1943-5606.0000666.
16. Saenger EH, Lebedev M, Uribe D, et al. Analysis of high-resolution X-ray computed tomography images of Bentheim sandstone under elevated confining pressures. Geophys Prospect. 2016;64:848–59. https://doi.org/10.1111/1365-2478.12400.
17. Gong L, Nie L, Xu Y. Geometrical and topological analysis of pore space in sandstones based on X-ray computed tomography. Energies. 2020;13:3774. https://doi.org/10.3390/en13153774.
18. Schmitt M, Halisch M, Müller C, et al. Classification and quantification of pore shapes in sandstone reservoir rocks with 3-D X-ray micro-computed tomography. Solid Earth. 2016;7:285–300. https://doi.org/10.5194/se-7-285-2016.
19. Terzis D, Laloui L. Cell-free soil bio-cementation with strength, dilatancy and fabric characterization. Acta Geotech. 2019;14:639–56. https://doi.org/10.1007/s11440-019-00764-3.
20. Akimana RM, Seo Y, Li L, et al. Exploring X-ray computed tomography characterization and reactive transport modelling of microbially-induced calcite precipitation in sandy soils. Am Soc Civil Eng. 2016. https://doi.org/10.1061/9780784480120.008.
21. Minto JM, Hingerl FF, Benson SM, et al. X-ray CT and multiphase flow characterization of a 'bio-grouted' sandstone core: the effect of dissolution on seal longevity. Int J Greenhouse Gas Control. 2017;64:152–62. https://doi.org/10.1016/j.ijggc.2017.07.007.
22. Roy N, Frost JD, Terzis D. 3-D contact and pore network analysis of MICP cemented sands. Granular Matter. 2023. https://doi.org/10.1007/s10035-023-01347-6.
23. Zhou B, Zhang X, Wang J, et al. Insight into the mechanism of microbially induced carbonate precipitation treatment of bio-improved calcareous sand particles. Acta Geotech. 2022. https://doi.org/10.1007/s11440-022-01625-2.
24. Wang B, Guo L, Luo X, et al. Identification and extraction of cementation patterns in sand modified by MICP: new insights at the pore scale. PLoS ONE. 2024;19:e0296437. https://doi.org/10.1371/journal.pone.0296437.
25. Terzis D, Laloui L. 3-D micro-architecture and mechanical response of soil cemented via microbial-induced calcite precipitation. Sci Rep. 2018;8:1416. https://doi.org/10.1038/s41598-018-19895-w.
26. Kirkland CM, Norton D, Firth O, et al. Visualizing MICP with X-ray μ-CT to enhance cement defect sealing. Int J Greenhouse Gas Control. 2019;86:93–100. https://doi.org/10.1016/j.ijggc.2019.04.019.
27. Huang M, Xu K, Liu Z, et al. Effect of drying-wetting cycles on pore characteristics and mechanical properties of enzyme-induced carbonate precipitation-reinforced sea sand. J Rock Mech Geotech Eng. 2023. https://doi.org/10.1016/j.jrmge.2022.12.032.
28. Zhao H, Zhao T, Ning Z, et al. Petrophysical characterization of tight oil sandstones by microscale X-ray computed tomography. Mar Pet Geol. 2019;102:604–14. https://doi.org/10.1016/j.marpetgeo.2019.01.029.
29. Schlüter S, Sheppard A, Brown K, et al. Image processing of multiphase images obtained via X-ray microtomography: a review. Water Resour Res. 2014;50:3615–39. https://doi.org/10.1002/2014WR015256.
30. Thomson P-R, Ellis R, Chiarella D, et al. Microstructural analysis from X-ray CT images of the brae formation sandstone, north sea. Front Earth Sci. 2020. https://doi.org/10.3389/feart.2020.00246.
31. Sun B, Hou S-S, Zeng S, et al. 3D characterization of porosity and minerals of low-permeability uranium-bearing sandstone based on multi-resolution image fusion. Nucl Sci Tech. 2020. https://doi.org/10.1007/s41365-020-00810-w.
32. Jacob A, Peltz M, Hale S, et al. Simulating permeability reduction by clay mineral nanopores in a tight sandstone by combining computer X-ray microtomography and focussed ion beam scanning electron microscopy imaging. Solid Earth. 2021;12:1–14. https://doi.org/10.5194/se-12-1-2021.
33. Su Y, Zha M, Jiang L, et al. Pore structure and fluid distribution of tight sandstone by the combined use of SEM, MICP and X-ray micro-CT. J Petrol Sci Eng. 2022;208:109241. https://doi.org/10.1016/j.petrol.2021.109241.
34. Whiffin VS. Microbial CaCO3 precipitation for the production of biocement. Perth: Murdoch University; 2004.
35. Erdmann N, de Payrebrune KM, Ulber R, et al. Optimizing compressive strength of sand treated with MICP using response surface methodology. SN Appl Sci. 2022. https://doi.org/10.1007/s42452-022-05169-8.
36. Deutsches Institut für Normung e. V. DIN EN ISO 17892–11:2021–03: Geotechnical investigation and testing - Laboratory testing of soil - Part 11: Permeability tests (ISO 17892–11:2019); German version EN ISO 17892–11:2019.
37. Buades A, Coll B, Morel J-M. Non-local means denoising. Image Proc Line. 2011;1:208–12. https://doi.org/10.5201/ipol.2011.bcm_nlm.
38. Darbon J, Cunha A, Chan TF, et al. Fast nonlocal filtering applied to electron cryomicroscopy. Piscataway: IEEE; 2008. p. 1331–4.
39. Lorensen WE, Cline HE. Marching cubes. In: Wolfe R, editor. Seminal graphics: pioneering efforts that shaped the field; [SIGGRAPH 98; celebrating 25 years of discovery; a publication of ACM SIGGRAPH]. New York: ACM Press; 1998. p. 347–53.

40. AlHomadhi ES. New correlations of permeability and porosity versus confining pressure, cementation, and grain size and new quantitatively correlation relates permeability to porosity. Arab J Geosci. 2014;7:2871–9. https://doi.org/10.1007/s12517-013-0928-z.
41. Cheshomi A, Mansouri S. Study the grain size and infiltration method effects for sand soil improvement using the microbial method. Geomicrobiol J. 2020;37:355–65. https://doi.org/10.1080/01490451.2019.1705437.
42. Song C, Wang C, Elsworth D, et al. Compressive strength of MICP-treated silica sand with different particle morphologies and gradings. Geomicrobiol J. 2022;39:148–54. https://doi.org/10.1080/01490451.2021.2020936.
43. Gowthaman S, Iki T, Nakashima K, et al. Feasibility study for slope soil stabilization by microbial induced carbonate precipitation (MICP) using indigenous bacteria isolated from cold subarctic region. SN Appl Sci. 2019. https://doi.org/10.1007/s42452-019-1508-y.
44. Zhao Y, Wang Q, Yuan M, et al. The effect of MICP on physical and mechanical properties of silt with different fine particle content and pore ratio. Appl Sci. 2022;12:139. https://doi.org/10.3390/app12010139.
45. Koval I, Roozbahani M, Frost D. Comparison between geometrical and dynamic particle packing. CRC Press; 2014.
46. Zhao Q, Li L, Li C, et al. A full contact flexible mold for preparing samples based on microbial-induced calcite precipitation technology. Geotech Test J. 2014;37:20130090. https://doi.org/10.1520/GTJ20130090.
47. Sun S, Shu L, Zeng Y, et al. Porosity–permeability and textural heterogeneity of reservoir sandstones from the lower cretaceous Putaohua member of Yaojia formation, Weixing oilfield, Songliao basin, northeast China. Mar Pet Geol. 2007;24:109–27. https://doi.org/10.1016/j.marpetgeo.2006.10.006.
48. Mahawish A, Bouazza A, Gates WP. Unconfined compressive strength and visualization of the microstructure of coarse sand subjected to different biocementation levels. J Geotech Geoenviron Eng. 2019. https://doi.org/10.1061/(ASCE)GT.1943-5606.0002066.
49. Hoang T, Alleman J, Cetin B, et al. Engineering properties of biocementation coarse- and fine-grained sand catalyzed by bacterial cells and bacterial enzyme. J Mater Civ Eng. 2020. https://doi.org/10.1061/(ASCE)MT.1943-5533.0003083.
50. Liu L, Liu H, Stuedlein AW, et al. Strength, stiffness, and microstructure characteristics of biocemented calcareous sand. Can Geotech J. 2019;56:1502–13. https://doi.org/10.1139/cgj-2018-0007.
51. Dadda A, Geindreau C, Emeriault F, et al. Characterization of contact properties in biocemented sand using 3D X-ray micro-tomography. Acta Geotech. 2019;14:597–613. https://doi.org/10.1007/s11440-018-0744-4.
52. Dadda A, Geindreau C, Emeriault F, et al. Characterization of microstructural and physical properties changes in biocemented sand using 3D X-ray microtomography. Acta Geotech. 2017;12:955–70. https://doi.org/10.1007/s11440-017-0578-5.
53. Wei-Soon Ng, Min-Lee Lee, Siew-Ling Hii (2012) An Overview Of The Factors Affecting Microbial-Induced Calcite Precipitation And Its Potential Application In Soil Improvement. Zenodo.
54. Maleki Kakelar M, Yavari M, Yousefi MR, et al. The influential factors in the effectiveness of microbial induced carbonate precipitation (MICP) for soil consolidation. J Hum Environ Health Promot. 2020;6:40–6. https://doi.org/10.2925/jhehp.6.1.8.
55. Wang Y, Soga K, DeJong JT, et al. A microfluidic chip and its use in characterising the particle-scale behaviour of microbial-induced calcium carbonate precipitation (MICP). Géotechnique. 2019;69:1086–94. https://doi.org/10.1680/jgeot.18.P.031.
56. Wang Y, Soga K, DeJong JT, et al. Microscale visualization of microbial-induced calcium carbonate precipitation processes. J Geotech Geoenviron Eng. 2019;145:4019045. https://doi.org/10.1061/(ASCE)GT.1943-5606.0002079.
57. Almajed A, Lateef MA, Moghal AAB, et al. State-of-the-art review of the applicability and challenges of microbial-induced calcite precipitation (MICP) and enzyme-induced calcite precipitation (EICP) techniques for geotechnical and geoenvironmental applications. Crystals. 2021;11:370. https://doi.org/10.3390/cryst11040370.
58. Shenton D, Cendes Z. Three-dimensional finite element mesh generation using delaunay tesselation. IEEE Trans Magn. 1985;21:2535–8. https://doi.org/10.1109/TMAG.1985.1064165.
59. Dong H, Blunt MJ. Pore-network extraction from micro-computerized-tomography images. Phys Rev E Stat Nonlin Soft Matter Phys. 2009;80:36307. https://doi.org/10.1103/PhysRevE.80.036307.
60. Meyer F, Beucher S. Morphological segmentation. J Vis Commun Image Represent. 1990;1:21–46. https://doi.org/10.1016/1047-3203(90)90014-M.
61. Liang Y, Hu P, Wang S, et al. Medial axis extraction algorithm specializing in porous media. Powder Technol. 2019;343:512–20. https://doi.org/10.1016/j.powtec.2018.11.061.
62. Ben-Noah I, Hidalgo JJ, Dentz M. Efficient pore space characterization based on the curvature of the distance map. arXiv. 2024. https://doi.org/10.4855/arXiv.2403.12591.
63. Li Z, Wang YH, Chow JK, et al. 3D pore network extraction in granular media by unifying the Delaunay tessellation and maximal ball methods. J Petrol Sci Eng. 2018;167:692–701. https://doi.org/10.1016/j.petrol.2018.04.058.
64. Alatrash H, Velledits F. Comparing petrophysical properties and pore network characteristics of carbonate reservoir rocks using micro X-ray tomography imaging and microfacies analyses. Int J Geomath. 2024;15:1–29. https://doi.org/10.1007/s13137-023-00243-8.
65. Lindquist WB, Lee S-M, Coker DA, et al. Medial axis analysis of void structure in three-dimensional tomographic images of porous media. J Geophys Res. 1996;101:8297–310. https://doi.org/10.1029/95jb03039.
66. Lindquist WB, Venkatarangan A. Investigating 3D geometry of porous media from high resolution images. Phys Chem Earth Part A. 1999;24:593–9. https://doi.org/10.1016/S1464-1895(99)00085-X.
67. Gao S, Meegoda JN, Hu L. Two methods for pore network of porous media. Num Anal Meth Geomechanics. 2012;36:1954–70. https://doi.org/10.1002/nag.1134.
68. Al-Raoush R, Thompson K, Willson CS. Comparison of network generation techniques for unconsolidated porous media. Soil Sci Soc Am J. 2003;67:1687–700. https://doi.org/10.2136/sssaj2003.1687.
69. Beucher S. The watershed transformation applied to image segmentation. Scan Microsc. 1992;1992:299–314.